J. Earth Planet. Sci. Nagoya Univ., Vol. 57, 19 to 41, 2010

CHIME geochronology of granitic gneiss from Baekdong in the Hongseong area of the Gyeonggi Massif, South Korea

Kazuhiro SUZUKI[1*], Ueechan CHWAE[2], Daniel J. DUNKLEY[3], Sung-Won KIM[2], Izumi KAJIZUKA[1] and Masayo MINAMI[1]

[1]The Center for Chronological Research, Nagoya University, Chikusa-ku, Nagoya 464-8602, Japan
[2]Korea Institute of Geoscience and Mineral Resources, 92 Gwahang-no, Yuseong-gu, Daejeon, 305-350, South Korea
[3]National Institute of Polar Research, 10-3 Midoricho, Tachikawa, Tokyo 190-8513, Japan
(Received November 10, 2010 / Accepted December 10, 2010)

ABSTRACT

CHIME dating was carried out on zircon and allanite in a sample of granitic gneiss from the Deokjeongri Granitic Gneiss, exposed at Baekdong (36°33.521'N, 126°44.131'E) in the Hongseong area, which lies in the southwestern part of the Gyeonggi Massif. Geochemically, the sample belongs to the high-K calc-alkaline series or shoshonite series of A-type granites, and is typical of within-plate granitoids. The CHIME ages for concentrically-zoned zircon cores and the core of an exceptionally large allanite grain are 824±29 Ma and 825±110 Ma, respectively. Outer growth zones in zircon with low Y_2O_3 and margins with high Y_2O_3 yield poorly defined ages of ca. 500 Ma and 230 Ma, respectively. Allanite rims give ages which cluster along two isochrons, 438±99 Ma for low-Y_2O_3 domains in equilibrium with Ca-rich garnet, and 254±30 Ma for high Y_2O_3 domains that formed during the breakdown of garnet. The present sample differs from granitic gneisses in the same lithological unit from other sites, in terms of both ages and geochemistry. Such diversity suggests that the Deokjeongri Granitic Gneiss is a composite unit, comprised of a variety of protoliths from differing tectonic environments and with differing tectonometamorphic histories.

INTRODUCTION

The Gyeonggi massif is located in the middle Korean Peninsula and is terminated by the Okcheon Belt to the south and by the Imjingang Fold Belt to the north (Fig. 1). The Hongseong area in the southwestern part of the massif has attracted much attention after the discovery of high-pressure garnet amphibolite (Oh *et al.*, 2002, 2005; Guo *et al.*, 2004). The garnet amphibolite is regarded as a retrogressed eclogite, since it retains remnants of omphacitic pyroxene in resorbed garnet porphyroblasts, and shows evidence of metamorphism at ultra-high pressure eclogite-facies conditions (1.70–2.09 GPa and 835–860°C for Bibong, Oh *et al.*, 2005, Kim *et al.*, 2006; 2.3 GPa and ca. 1000°C for Baekdong, Oh *et al.*, 2009). It occurs together with marble and

*Corresponding author, e-mail: suzuki@nendai.nagoya-u.ac.jp

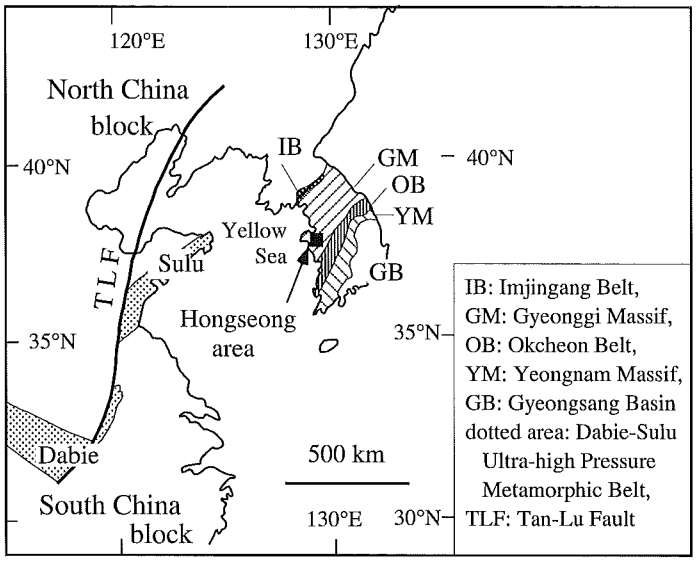

Fig. 1 Simplified tectonic map of Korea and adjacent areas (after Oh *et al.*, 2004). IB: Imjingang Belt, GM: Gyeonggi Massif, OB: Okcheon Belt, YM: Yeongnam Massif, GB: Gyeongsang Basin, dotted area: Dabie-Sulu Ultra-high Pressure Metamorphic Belt, TlF: Tan-Lu Fault

serpentinite as tectonic lenses in the Wolhyeonri Formation and the Deokjeongri Granitic Gneiss (Kim *et al.*, 2006; Oh *et al.*, 2009) and has yielded a SHRIMP zircon age of 231±3 Ma (Guo *et al.*, 2004) and a Sm-Nd internal isochron age of 225–258 Ma (Oh *et al.*, 2005). Kim *et al.* (2006, 2008) confirmed the Triassic age for eclogite-facies metamorphism through detailed SHRIMP dating of zircon. The lithological assemblage in the Hongseong area is similar to that in the Sulu Collisional Belt of China, which comprises ultramafic rocks, marble and Triassic ultra-high pressure metabasite within the granitic to tonalitic gneisses of the Jiaonan Gneiss Complex (Wang *et al.*, 1989; Zhang *et al.*, 1994; Kato *et al.*, 1997). The simultaneity of ultra-high pressure metamorphism suggests that the Hongseong area is an eastward extension of the Sulu Collisional Belt (Guo *et al.*, 2004; Oh *et al.*, 2005, 2006, 2009: Kim *et al.*, 2006, 2008).

The Wolhyeonri Formation contains, in addition to the retrogressed eclogite bodies, an amphibolite body that gives a 763.5±18.3 Ma age for the protolith formation and 435–375 Ma age for the amphibolite-facies metamorphism (Oh *et al.*, 2009). The Deokjeongri Granitic Gneiss has yielded SHRIMP U-Pb ages of ca. 815 Ma or 335–473 Ma for zircon cores and 223–235 Ma for zircon overgrowths (Cho, 2001). For granitic gneiss at Baekdong, Kim *et al.* (2006) reported 940–395 Ma ages for zircon cores and ca. 420 Ma ages for zircon overgrowths and unzoned zircon grains, together with a 241.5±5.2 Ma K-Ar biotite age. They pointed out that there is no evidence for zircon growth or isotopic disturbance in the Triassic, when the retrogressed eclogite hosted in the granitic gneiss was metamorphosed. This contrasts with ages from amphibole-bearing orthogneiss reported by Kim *et al.* (2008), which include a well-defined 839±10 Ma age for zircon cores and a poorly defined age of 229±10 Ma for zircon overgrowths, but no evidence of zircon growth at ca. 420 Ma. Such contrasting ages

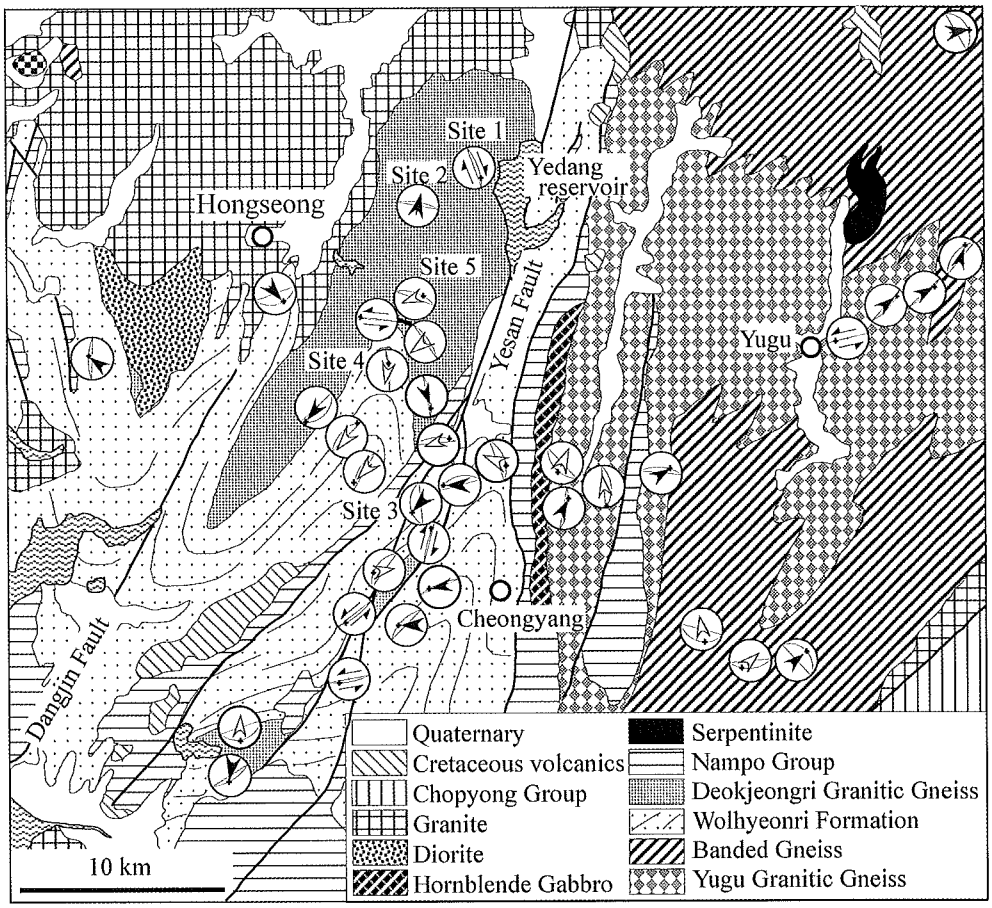

Fig. 2 Schematic geological map of the Hongseong area (simplified from Lee *et al.*, 1996 with modification of Oh *et al.*, 2004 and Kim *et al.*, 2006, 2008) showing the location of analyzed sample and stereographic projections of foliation and lineation. Black arrow indicates direction of synthetic shear, and white arrow antithetic shear.

lead to the question whether the whole of the Deokjeongri Granitic Gneiss underwent both ca. 420 Ma metamorphism and Triassic high-pressure metamorphism, or if it is geologically composite in nature, comprising blocks with disparate histories that were amalgamated after Triassic metamorphism. Confirmation of the variety of ages in the Deokjeongri Granitic Gneiss is also important for correlating the Hongseong area with the Sulu Collision Belt.

To look for evidence of a ca. 420 Ma event as well as Triassic metamorphism, we examined zircon and allanite from the Deokjeongri Granitic Gneiss exposed at Baekdong (site 5 in Fig. 2; 36 33.521'N, 126 44.131'E) by the Chemical Isochron Method (CHIME), which involves micron-scale dating of Th- and U-bearing accessory minerals through precise chemical analyses using an electron probe microanalyzer (Suzuki *et al.*, 1991; Suzuki and Adachi, 1991). This paper reports CHIME dating of the Deokjeongri Granitic Gneiss, together with sample petrography and whole-rock chemistry, and discusses the tectonic implications of the results.

GEOLOGICAL SETTING

The Hongseong area comprises metamorphic rocks, granitic, dioritic and gabbroic intrusives, Jurassic Nampo Group sediments, Cretaceous volcanics and Quaternary cover (Fig. 2, Lee *et al.*, 1996; Oh *et al.*, 2004; Kim *et al.*, 2006, 2008). Most intrusives had been regarded to be of Jurassic, but Seo *et al.* (2010) recently pointed out that the diorite at the SW of Hongseong (Gwangcheon complex) is a composite intrusion of Triasic mangerite (232±3 Ma) and syenite (230±3 Ma). The Nampo Group

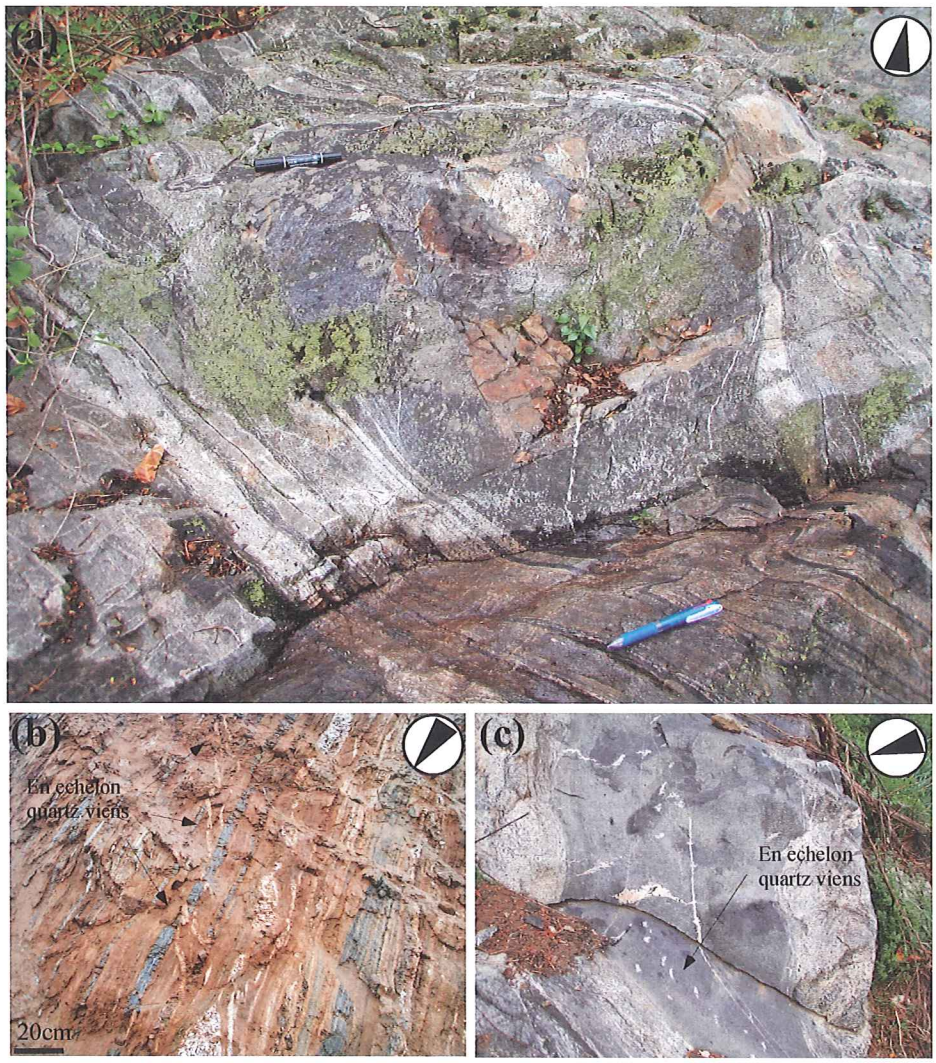

Fig. 3 (a) Sinistral rotation of amphibole-rich block within a conformable metasediment lens near the sampling site (site 5). (b) Boudinage with dextral shearing and en echelon veining in metasediment of the Wolhyeonri Formation (site 4). (c) Foliated hornblende-dominated tonalitic gneiss and a mafic dyke at site 2. En echelon veins in the dyke show dextral shear, whereas minerals in N-dipping foliation show synthetic shear. Arrow points to north.

nonconformably overlies the metamorphic rocks and is folded into synclinal structure with a NE-SW axial trace. Parts of the Nampo Group were metamorphosed by the intrusion of Jurassic granites.

The metamorphic rocks are subdivided on the basis of field occurrence and lithology into the Wolhyeonri Formation and the Deokjeongri Granitic Gneiss to the west, and the banded gneisses and the Yugu Granitic Gneiss to the east. The Wolhyeonri Formation is exposed in an S-shaped area between the Dangjin and Yesan Faults. It consists of biotite schist, garnet-amphibolite and marble. Most amphibolite bodies are interpreted as tectonic lenses within biotite schist (Oh *et al.*, 2009). The Deokjeongri Granitic Gneiss is predominantly composed of amphibole-bearing granitic orthogneiss, biotite-bearing granitic orthogneiss, amphibole-dominated tonalitic orthogneiss and leucogranitic orthogneiss. These gniesses enclose isolated lenticular bodies of garnet amphibolite (retrogressed eclogite), serpentinized ultramafic rock and marble. The banded gneiss is composed mainly of biotite gneiss, quartzofeldspathic gneiss and migmatite. The Yugu Granitic Gneiss is medium to coarse grained with a gneissosity defined by alternating biotite-rich mafic and felsic layers, with sporadic augen structures. The gneiss typically lacks amphibole, consisting mainly of quartz, plagioclase, K-feldspar and biotite with or without garnet. Garnet is typically surrounded by pinite.

The foliation in the Deokjeongri Granitic Gneiss at the sampling site (Site 5) trends WNW-ESE and dips 63° N. The foliation contains a prominent mineral lineation that plunges 50° NE. Asymmetric porphyroclasts of feldspar suggest a top-to-the-SW shear sense. An amphibolite block wrapped by gneissosity in the host metasediment shows sinistral rotation (Fig. 3a). This is consistent with the shear sense in the host granitic gneiss, but the sinistral rotation likely predates the top-to-the-SW shear. The foliation in the Deokjeongri Granitic Gneiss is generally sub-parallel to that in marble (site 1) and serpentinite (site 6) lenses. The Wolhyeonri Formation has a steeply dipping (>50°) foliation that transposes sedimentary bedding. Metasediments of the Wolhyeonri Formation at site 4 are boudinaged with a dextral (top-to-the-SSW) shear sense and contains secondary en-echelon veins that show sinistral (top-to-the-ENE) shear sense (Fig. 3b). Amphibole-dominated tonalitic orthogneiss exposed at site 2 has different shear sense, synthetic in the earlier stage (mineral alignment) and dextral shear in the later stage (en-echelon veins) (Fig. 3c). The Yugu gneiss and banded gneiss contains a mineral lineation trending NE-SW with gentle plunges and exhibits a top-to-the-NE shear sense (Fig. 2).

PETROGRAPHY OF THE GRANITIC GNEISS

The granitic gneiss is light gray and medium-grained with a distinctive gneissosity. The main constituent minerals are quartz, microcline, oligoclase, biotite, hornblende and garnet. Accessory minerals include allanite, zircon, apatite and xenotime. Biotite is partly replaced by chlorite. Quartz is strained or recrystallized into grain aggregates of 0.05–0.4 mm in size and aligned parallel to the foliation. Microcline porphyroclasts up to 3 mm in size were deformed, fragmented along margins, and re-aligned with oligoclase and recrystallized quartz. Oligoclase grains underwent significant recrystallization.

Table 1. Electron microprobe analyses of constituent minerals in granitic gneiss from site 5

	Kfs	Kfs	Pl	Pl	Grt-c	Grt-c	Grt-r	Grt-r	Bt	Bt	Bt (grt)	Hb	Hb
SiO_2	65.12	64.92	63.90	64.39	37.37	37.25	37.00	36.92	33.02	33.50	32.41	40.08	39.66
TiO_2	0.00	0.00	0.00	0.00	0.00	0.00	0.00	0.00	4.55	3.75	3.26	1.19	1.30
Al_2O_3	18.40	18.33	22.17	22.12	20.45	20.80	20.45	20.72	13.43	13.81	14.98	11.18	10.71
Cr_2O_3	0.00	0.00	0.00	0.00	0.00	0.00	0.00	0.00	0.00	0.00	0.00	0.00	0.00
Fe_2O_3	0.04	0.05	0.17	0.13	1.13	0.46	0.77	0.17	–	–	–	–	–
FeO	–	–	–	–	27.67	29.18	28.85	29.27	33.94	33.41	32.65	28.46	29.39
MnO	0.00	0.00	0.00	0.00	0.80	0.95	3.09	4.24	0.23	0.18	0.15	0.31	0.32
MgO	0.00	0.00	0.00	0.00	0.27	0.42	0.23	0.23	0.95	1.20	1.42	3.10	2.58
NiO	0.00	0.00	0.00	0.00	0.00	0.00	0.00	0.00	0.00	0.00	0.00	0.00	0.00
CaO	0.00	0.00	3.47	3.22	12.06	10.79	9.29	7.71	0.00	0.02	0.05	10.59	10.69
BaO	0.08	0.14	0.00	0.00	0.00	0.00	0.00	0.00	0.10	0.10	0.12	0.00	0.00
Na_2O	1.14	1.33	9.46	9.59	0.00	0.00	0.00	0.00	0.00	0.05	0.06	1.56	1.56
K_2O	15.18	14.83	0.28	0.24	0.00	0.00	0.00	0.00	8.31	8.85	7.97	1.36	1.41
H_2O	0.00	0.00	0.00	0.00	0.00	0.00	0.00	0.00	3.59	3.61	3.57	1.88	1.86
Total	99.95	99.60	99.45	99.69	99.75	99.85	99.68	99.26	98.13	98.48	96.61	99.71	99.48
O=	8	8	8	8	12	12	12	12	22	22	22	23	23
Si	3.001	3.001	2.839	2.848	3.007	2.997	2.999	3.005	5.505	5.554	5.444	6.396	6.388
Ti	0.000	0.000	0.000	0.000	0.000	0.000	0.000	0.000	0.570	0.468	0.412	0.142	0.157
Al	0.999	0.999	1.161	1.153	1.931	1.972	1.953	1.988	2.638	2.699	2.965	2.103	2.034
Cr	0.000	0.000	0.000	0.000	0.000	0.000	0.000	0.000	0.000	0.000	0.000	0.000	0.000
Fe^{3+}	0.001	0.002	0.006	0.004	0.069	0.028	0.047	0.012	–	–	–	0.000	0.000
Fe^{2+}	–	–	–	–	1.863	1.963	1.955	1.993	4.732	4.632	4.586	3.799	3.960
Mn	0.000	0.000	0.000	0.000	0.055	0.064	0.212	0.292	0.033	0.025	0.021	0.042	0.044
Mg	0.000	0.000	0.000	0.000	0.033	0.050	0.028	0.033	0.237	0.297	0.355	0.737	0.620
Ni	0.000	0.000	0.000	0.000	0.000	0.000	0.000	0.000	0.000	0.000	0.000	0.000	0.000
Ca	0.000	0.000	0.165	0.153	1.035	0.930	0.807	0.672	0.000	0.004	0.009	1.811	1.846
Ba	0.001	0.003	0.000	0.000	0.000	0.000	0.000	0.000	0.007	0.006	0.008	0.000	0.000
Na	0.102	0.119	0.814	0.823	0.000	0.000	0.000	0.000	0.000	0.015	0.018	0.483	0.487
K	0.892	0.875	0.016	0.013	0.000	0.000	0.000	0.000	1.766	1.872	1.707	0.277	0.290

Garnet occurs in subhedral porphyroblasts 0.2–1.1 mm in across and surrounded by an aggregate of plagioclase and biotite. Most garnet grains contain quartz and biotite inclusions that show random distribution. Feldspars and hornblende inclusions are rare. The marginal portions are relatively free from inclusions and are partly altered to biotite. Most biotite flakes and hornblende prisms, 0.1–0.6 mm in length, have a film-like arrangement and define the mineral lineation in the foliation. Allanite forms typically prisms of 0.2–0.3 mm in length with an exceptionally large equant grain of ca. 1.2 mm in across. Allanite prisms are aligned parallel to the mineral lineation and the large grain is likely a porphyroclast. Zircon occurs as fine- to medium-grained prisms (0.05–0.15 mm in length) with aspect ratio of 1.3 to 7. Most grains are well faced, but some show rounded form. Xenotime, smaller than 2 μm across, occurs in the plagioclase and biotite aggregate around garnet.

The EPMA analyses of constituent minerals are listed in Table 1. Total iron in K-feldspar and plagioclase was assumed to be ferric and that in biotite and hornblende was assumed to be ferrous. Ferric iron in garnet was estimated to ensure $Al+Fe^{3+}$ = 2 pfu on the basis of O=12.

Microcline contains little CaO (below the detection limit at the 2σ confidence level,

0.02 wt%) and Fe_2O_3 (< 0.05 wt%) but detectable amounts of BaO (Table 1). The BaO contents are as high as 0.14 wt%. Compositional variation of microcline is limited, with $Or_{88}Ab_{12}$ to $Or_{90}Ab_{10}$. Plagioclase contains little K_2O (0.2– 0.3 wt% corresponding to $Or_{1.3}$– $Or_{1.6}$) and BaO (below the detection limit at the 2σ confidence level, 0.04 wt%). Compositional ranges are An_{17}-An_{15}.

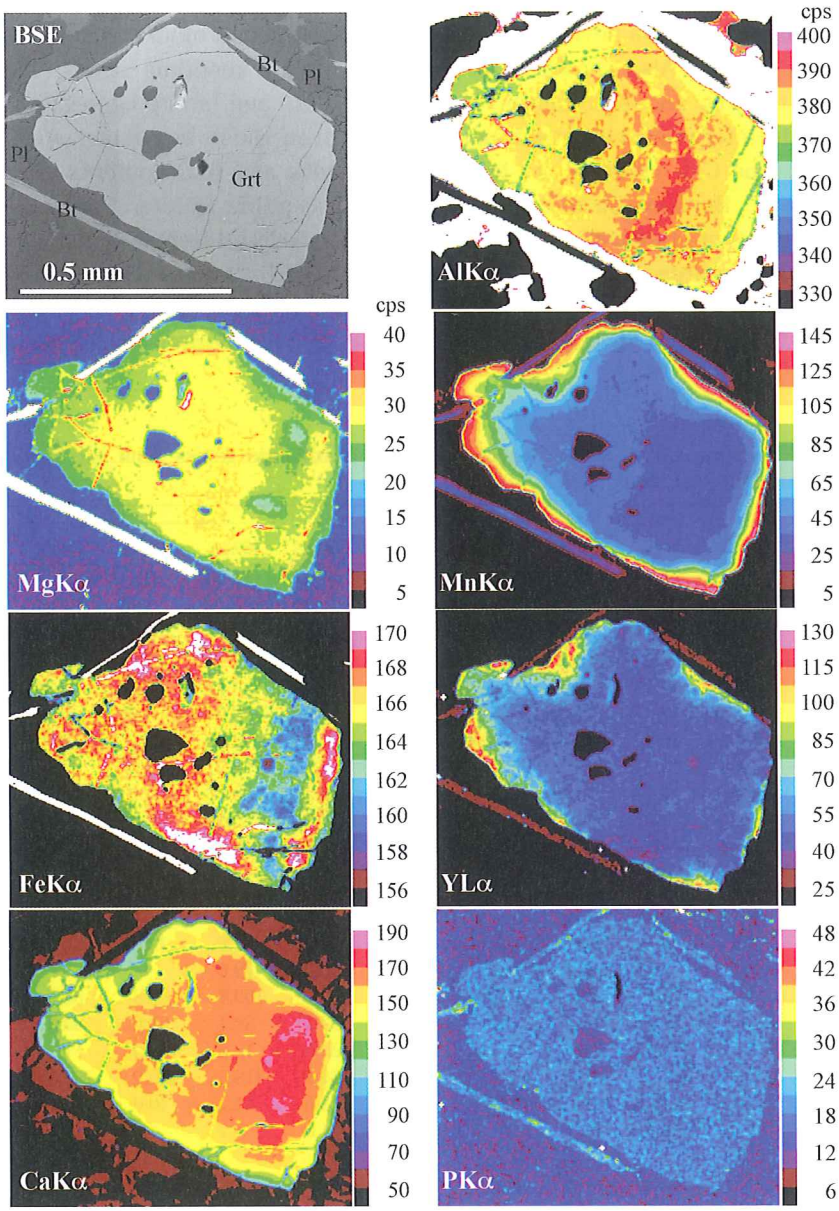

Fig. 4 BSE image and X-ray intensity maps of a garnet grain. Analytical conditions for mapping were 15 kV, 200–300 nA and 1–2s dwell time.

Garnet has relatively high CaO. While Si-cations approaches 3 per 12 oxygens, Al-cations slightly fall below 2 along with divalent cations (Fe, Mn, Mg and Ca) over 3. This suggests presence of a substantial andradite component. Garnet compositions are $Alm_{65.3}Sps_{2.1}Prp_{1.7}Grs_{29.6}Adr_{1.4}$ for the most Mg-rich domain and $Alm_{66.6}Sps_{9.8}Prp_{1.1}Grs_{21.9}Adr_{0.6}$ for the rim. The most Ca-rich domain ($Alm_{62.4}Sps_{1.8}Prp_{1.1}Grs_{31.4}Adr_{3.3}$) shows the lowest concentrations of Mg and Mn (Fig. 4). The Ca content decreases from the core to rim along with the decreasing in Mg and the increasing in Fe and Mn. The Y content is exactly covariant with the Mn content (Fig. 4). The element mapping shows development of the plagioclase and biotite aggregate around the garnet grains. Also shown is the presence of tiny xenotime grains (see lower central in the YLα and PKα images) in the plagioclase and biotite aggregate. Biotite shows little inter-grain compositional variation even those in contact with garnet (Table 1). The CaO contents are less than 0.05 wt%, and BaO contents are as high as 0.12 wt.%. Because Ba in biotite is highly susceptible to alteration and can be lost prior to other compositional changes in octahedral and tetrahedral sheets in the biotite structure (Adachi *et al.*, 1998), the amounts of BaO and K_2O (normally larger 1.7 pfu, O=22) suggest that biotite underwent little alteration. The Fe/(Fe+Mg) ratios are 0.94–0.95 for biotite distant from garnet and c. 0.92 for biotite close to garnet. The

Table 2. XRF analyses of granitic gneiss from site 5, tonalitic gneiss from site 2 and garnet amphibolites from sites 1, 3 and 4.

	Site 5	Site 2	Site 1	Site 3			Site 4			
	605A	602B	601B	603A	603B	603C	604A	604B	604C	604D
SiO_2 (%)	75.14	56.20	49.11	49.34	49.43	48.68	50.09	43.50	43.86	45.64
TiO_2	0.23	0.81	1.01	0.72	0.83	0.81	0.39	2.46	4.27	1.27
Al_2O_3	12.63	18.26	18.10	14.14	13.53	14.89	16.92	13.93	14.34	16.66
FeO*	2.10	7.72	8.03	11.54	12.73	11.99	7.25	20.18	18.84	12.41
MnO	0.03	0.13	0.12	0.17	0.20	0.17	0.13	0.20	0.24	0.17
MgO	0.14	3.08	4.60	8.20	8.19	7.80	8.94	6.53	5.92	8.88
CaO	0.66	6.87	12.69	11.96	11.72	13.25	13.23	11.62	9.54	11.76
Na_2O	2.68	4.21	2.01	2.69	2.39	2.10	2.27	1.88	2.56	1.88
K_2O	5.59	1.79	2.69	0.97	1.14	0.79	0.42	0.12	0.45	0.07
P_2O_5	0.04	0.31	0.13	0.03	0.04	0.04	0.02	0.02	0.07	0.02
Total	99.24	99.38	98.49	99.76	100.20	100.52	99.66	100.44	100.09	98.76
V (ppm)	3.7	168.0	214.8	292.7	279.9	288.4	165.3	796.8	421.5	319.8
Cr	8.1	24.9	27.8	–	304.6	332.0	222.5	29.1	1.4	165.3
Co	3.7	33.7	29.1	51.9	60.4	51.3	34.0	42.8	56.0	52.9
Ni	2.0	–	44.2	132.6	117.2	119.8	70.0	–	–	76.8
Cu	–	52.5	10.9	145.8	77.6	107.8	103.3	62.8	58.5	112.0
Zn	49.9	77.7	125.7	78.7	86.1	79.1	38.1	98.0	89.9	75.2
Rb	179.3	55.4	105.1	46.6	36.0	29.0	18.5	4.0	11.5	0.3
Sr	101.9	768.1	853.3	188.7	156.4	156.8	418.1	189.9	283.7	295.6
Y	46.1	19.4	22.2	20.9	23.1	23.5	11.1	10.6	10.8	16.7
Zr	343.7	28.2	47.9	19.2	25.3	24.0	5.7	6.0	15.9	5.2
Nb	33.8	–		–	–	–	–	–	–	–
Ba	839.7	433.3	544.2	130.9	343.9	277.7	68.1	23.8	288.6	42.6
Pb	30.9	11.2	14.9	6.5	3.6	5.2	4.3	1.8	3.5	4.7
Th	22.8	–	–	1.8	–	–	–	–	–	–

FeO*: total Fe as ferrous iron

Si, Al, Ca and Na+K contents of amphibole are around 6.39, 2.10, 1.83 and 0.75 per 23 oxygens, respectively. It is ferro-pargasitic hornblende, following the nomenclature of Leake *et al.* (1997).

The XRF analysis of the present sample is listed in Table 2, together with the analyses of hornblende-bearing tonalitic gneiss collected from the west of Yadong Reservior (Site 2) and garnet amphibolite from sites 1, 3 and 4. The granitic gneiss sample has 75.14 wt.% SiO_2 with 5.59 wt.% K_2O. The slightly peraluminous chemistry ($Al_2O_3/(CaO+Na_2O+K_2O)$ = 1.08) is consistent with the presence of biotite and garnet with a small amount of hornblende. The granitic gneiss shows high concentrations of Rb, Zr, Y, and Nb compared with the tonalitic gneiss.

CHIME DATING OF ZIRCON AND ALLANITE

Zircon and allanite grains in polished thin sections were analyzed using the JEOL JCXA-733 electron microprobe equipped with 4 wavelength dispersive spectrometers with 140 mm-radius Rowland circles. Each spectrometer was equipped with a PET (002 pentaerythritol) diffraction crystal and a sealed Xe X-ray detector. Instrumental operating conditions for spot analysis were 15 kV accelerating voltage, 3–10 μm probe diameter and 150 nA probe current. ThMα, UMβ, PbMβ and YLγ lines were measured simultaneously for zircon analyses and PbMα instead of PbMβ was measured for allanite analyses. X-ray intensity was integrated over 600–800s for line peak position and over 300–400s period for two optimal background positions. The detection limits at a 2σ confidence level were 0.0043, 0.0065 and 0.0038 wt.% for ThO_2, UO_2 and PbO, respectively. Relative errors (% sd) for the present Pb determinations of zircon (0.0046–0.0470 wt.% PbO) and allanite (0.0057–0.0829 wt.% PbO) are approximated by $0.459\times C^{-0.956}$ (R=0.99) and $0.907\times C^{-0.782}$ (R=0.99), respectively, where C represents PbO concentration in wt.%. Relative errors for U and Th determinations are $0.797\times C^{-0.923}$ and $0.271\times C^{-0.954}$, respectively for zircon, and $0.920\times C^{-0.787}$ and $0.631\times C^{-0.725}$, respectively for allanite. The analyses are listed in Table 3.

Compositional maps of zircon grains are given in Figs. 5 and 6. Zircon grains comprise concentrically-zoned domains, compositionally patchy domains, compositionally uniform domains and marginal domains. Grain Z01 (Fig. 5) consists of a patchy, inclusion-rich core, surrounded by concentrically-zoned zircon with a compositionally uniform outer zone (right end) and narrow, planar marginal domains (lower end and part of upper end). Within the core and concentrically-zoned domains, UO_2 contents range from 0.012 to 0.336 wt.%, ThO_2 from 0.005 to 0.087 wt.% and Y_2O_3 contents from 0.046 to 0.37 wt.%, with Th/U values of 0.002–0.693. The compositionally uniform domain (spots 19, 20 and 23) is characterized by low Th/U (<0.07) and Y_2O_3 (<0.015 wt.%). The marginal domain is characterized by high YLα counts (Spots 24 and 25, 2.6–4.8 wt.% Y_2O_3) that are covariant with PKα counts.

Zircon grain Z02 (Fig. 6) comprises concentrically-zoned domain (lower half) truncated by compositionally uniform domain (upper half). The latter (spots 04, 06, 08, 11 and 12) is characterized by low Th/U (<0.2) and Y_2O_3 (<0.024 wt.% with an exceptional 0.13 wt.% at Spot 06). Grains Z03 and Z04 consist of compositionally patchy domains (Fig. 6), with low UO_2 (<0.084 wt.%) and high Y_2O_3 concentrations

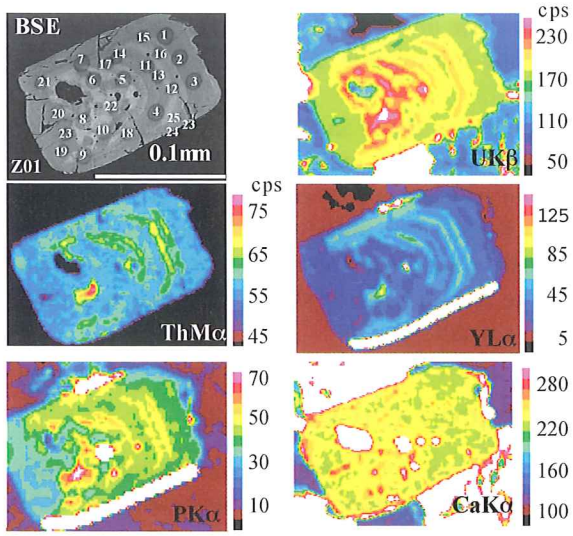

Fig. 5
BSE image and X-ray intensity maps of zircon grain Z01. Analytical conditions for this mapping were 15 kV, 400 nA and 5s dwell time for UMβ, ThMα and YLα, and 150 nA and 3s dwell time for PKα and CaKα. Pixel step was 3 μm.

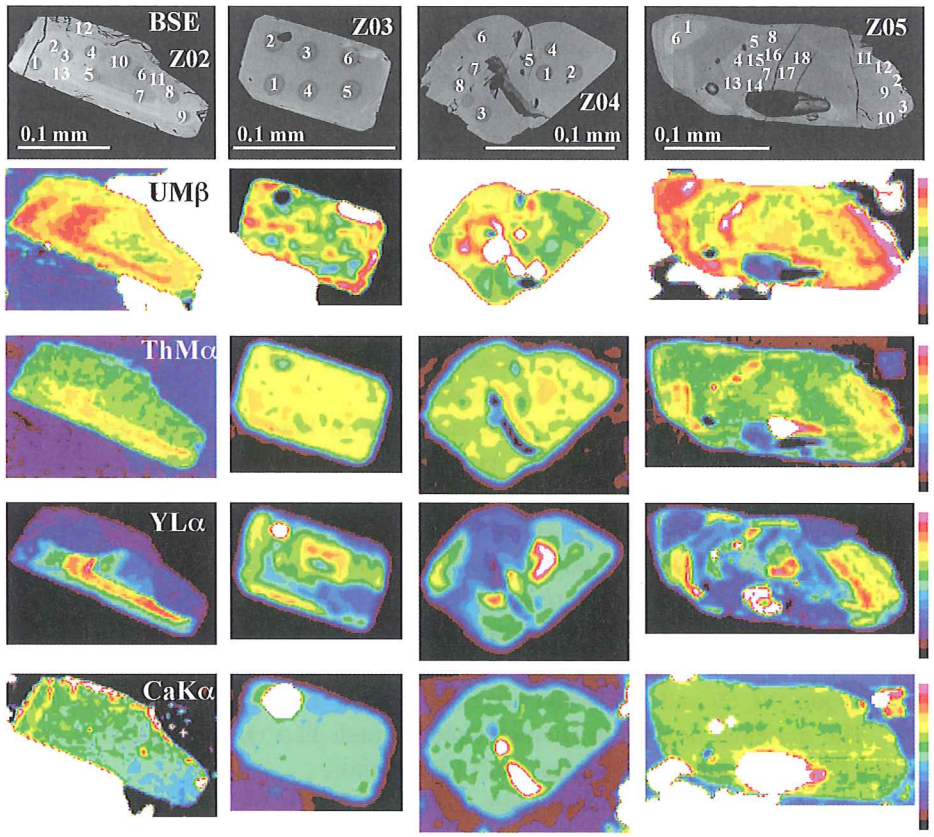

Fig. 6 BSE images and X-ray intensity maps of zircon grains Z02, Z03, Z04 and Z05. The UMβ, ThMα, YLα and CaKα intensities were measured simultaneously at 15k and 250–400 nA. Dwell time and pixel step were 5–10s and 3 μm, respectively. Different grains were mapped with different probe current, and color bars were not labeled.

(normally 0.105–0.441 wt.%, along with no detectable Y_2O_3 at spots 06 and 07 in grain Z04). Grain Z05 comprises concentrically-zoned domain with UO_2 contents from 0.050 to 0.363 wt.%, ThO_2 from 0.008 to 0.095 wt.% and Y_2O_3 contents from 0.067 to 0.158 wt.%, and Th/U values of 0.002–0.693.

Geisler and Schleicher (2000) showed that high Ca contents in zircon are indicative of alteration of radiation-damaged domains by low-temperature aqueous solutions. For the lowest chance of including damaged zircon with Pb loss in age estimates, zircon analyses were screened for CaO<0.015 and K_2O<0.015 (Suzuki and Kato, 2008). A total of 12 analyses out of screened 61 analyses contain no detectable amounts of Pb owing to their low UO_2 and ThO_2 concentrations. The remaining 49 analyses were classified into two groups, analyses with apparent ages older and younger than 750 Ma. The older group of ages comes from spots within concentrically-zoned and patchy domains (Fig. 7, upper). Analyses with <750Ma apparent ages were encountered mostly within compositionally homogeneous outer domains, but also from the patchy core of grain Z01. A single 229 Ma spot was measured on the right marginal zone of grain

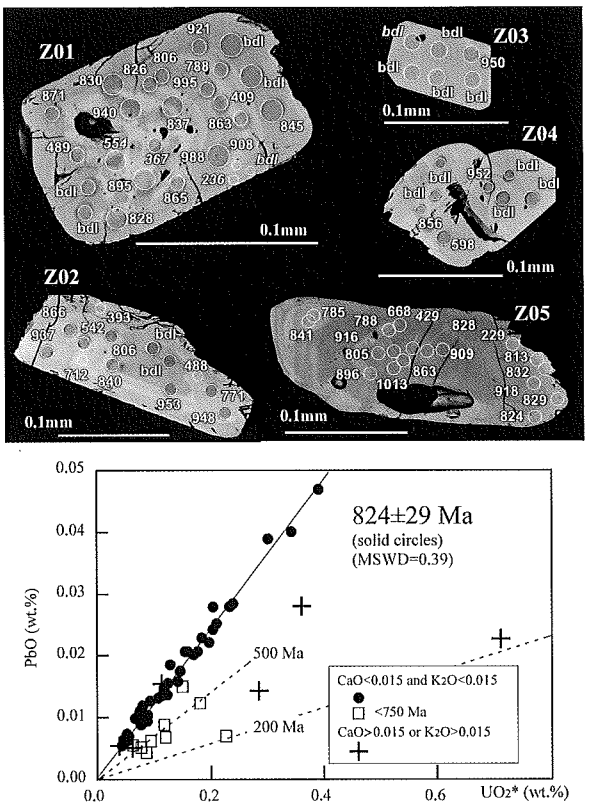

Fig. 7 Apparent ages of analyzed spots (above) and PbO-UO_2* (the measured UO_2 plus UO_2 equivalent of the measured ThO_2) plots of zircon analyses. bdl; the PbO content below the detection limit. Circle and square represent data points screened with the chemical criteria CaO<0.015 and K_2O<0.015, and crosses show rejected data points. Data points shown by circles were used for the calculation of the 824±29 Ma age.

Z05 (Fig. 7, upper). Data with apparent ages older than 750 Ma define an isochron of 824±29 Ma with an intercept of 0.0008±0.0007 (Fig. 7, lower). Five data points with apparent ages around 500 Ma give a less well-defined isochron of 505±125 Ma with an intercept of -0.0008±0.0033. The Y- and P-rich margin of grain Z01 (spot 25) and the periphery of grain Z05 (spot 11) give Triassic ages. The negligible amount of Ca and K in spot 11 of grain Z05 is consistent with the 229 Ma age as a growth age, rather than Pb loss from damaged zircon.

Three grains of allanite, comprising porphyroblast A01 and matrix grains A02 and A03, were examined. Grain A01 has complex zoning, with Th-rich patches dominating the grain centre (lighter domains in the backscattered electron image, Fig. 8, upper left) and lower Th patches on the margins, both intergrown with other minerals. In lighter (high-BSE response) domains, ThO_2, UO_2 and Y_2O_3 concentrations range from 1.850 to 0.919 wt.%, from 0.167 to 0.04 wt.% and from 0.597 to 0.359 wt.%, respectively, whereas in darker domains they range from 1.442 to 0.517 wt.%, from 0.243 to 0.004 wt.% and from 0.661 to 0.368 wt.%, respectively. Within the darker domains, spots with younger apparent ages tend to contain higher Y_2O_3 than older spots (>300 Ma, lower left of Fig. 8). Allanite has a solid solution relationship with a Pb-bearing end-member, hancockite ($(Ca,Pb,Sr)_2(Al,Fe^{3+})_3(SiO_4)(Si_2O_7)(OH)$; Dunn, 1985). Most rim analyses of matrix allanite (*e.g.* A03 in Table 3) contain considerable initial Pb.

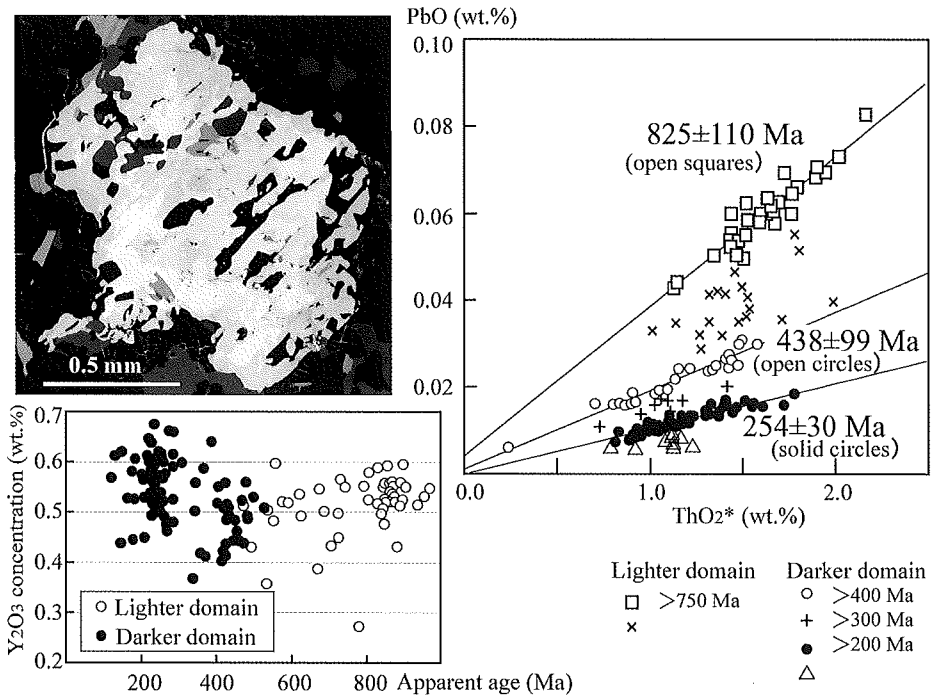

Fig. 8 BSE image of A01 prophyroblastic allanite (upper left); plot of Y_2O_3 concentration against apparent age (lower left), and PbO -ThO_2* plots (ThO_2* = ThO_2 plus ThO_2 equivalent of measured UO_2) of allanite analyses.

Table 3. (continued)

	ThO_2	UO_2	PbO	Age	UO_2*	CaO	Y_2O_3	S	K_2O
Z05-01	0.0111	0.1192	0.0138	785	0.1225	–	0.0088	–	–
Z05-02	0.0955	0.3633	0.0470	832	0.3914	–	0.1365	–	0.0027
Z05-03	0.0509	0.2199	0.0281	829	0.2349	0.0034	0.0748	–	0.0000
Z05-04	0.0303	0.0688	0.0090	805	0.0777	0.0078	0.0835	–	0.0033
Z05-05	0.0804	0.1732	0.0223	788	0.1970	0.0079	0.1589	–	0.0070
Z05-06	0.0149	0.1636	0.0204	841	0.1680	–	0.0099	–	0.0031
Z05-07	0.0219	0.0496	0.0070	863	0.0560	0.0030	0.0827	–	0.0078
Z05-08	0.0176	0.0560	0.0058	668	0.0613	0.0053	0.0678	–	–
Z05-09	0.0467	0.1412	0.0207	918	0.1549	0.0064	0.1373	–	–
Z05-10	0.0462	0.1902	0.0242	824	0.2038	0.0068	0.0965	–	–
Z05-11	0.0668	0.2044	0.0070	229	0.2250	0.0038	0.1172	–	0.0033
Z05-12	0.0877	0.3173	0.0402	813	0.3432	0.0063	0.1365	0.0042	0.0025
Z05-13	0.0084	0.1565	0.0207	896	0.1590	0.0078	0.0156	–	0.0052
Z05-14	0.0238	0.0736	0.0120	1013	0.0805	0.0080	0.0784	–	0.0059
Z05-15	0.0315	0.0703	0.0106	916	0.0795	0.0071	0.0879	–	–
Z05-16	0.0256	0.0697	0.0046	429	0.0775	0.0149	0.0772	–	0.0089
Z05-17	0.0676	0.0931	0.0135	828	0.1130	0.0072	0.1335	–	0.0052
Z05-18	0.0305	0.0659	0.0099	909	0.0748	0.0064	0.1442	–	0.0023

	ThO_2	UO_2	PbO	Age	ThO_2*	CaO	Y_2O_3	S	K_2O
A01-001D	0.8157	0.0355	0.0099	251	0.9308	11.44	0.6177	0.0018	0.0042
A01-002D	0.7401	0.1504	0.0131	252	1.2278	12.04	0.5247	–	–
A01-003D	0.8255	0.0040	0.0162	462	0.8387	11.43	0.4444	–	–
A01-004D	0.7978	0.0040	0.0071	210	0.8107	11.64	0.5661	0.0024	–
A01-005D	1.5763	0.1216	0.0397	472	1.9773	7.97	0.5146	–	–
A01-006D	1.3763	0.0618	0.0299	445	1.5797	8.96	0.4451	0.0073	0.0028
A01-007D	1.1535	0.0682	0.0133	229	1.3743	9.58	0.5397	0.0053	0.0086
A01-008D	0.8869	0.0889	0.0110	221	1.1745	11.08	0.5342	0.0055	0.0074
A01-009D	1.2758	0.0590	0.0251	402	1.4693	9.19	0.5175	0.0080	0.0037
A01-010D	1.2298	0.0985	0.0159	243	1.5490	9.15	0.5207	0.0102	0.0032
A01-011D	0.8197	0.0363	0.0084	212	0.9371	12.97	0.5324	0.0022	–
A01-012D	0.8144	0.0957	0.0063	133	1.1220	11.79	0.6126	–	0.0055
A01-013D	0.7890	0.0779	0.0190	428	1.0450	11.94	0.4840	–	–
A01-014D	0.8122	0.0723	0.0104	235	1.0464	11.67	0.5550	–	0.0033
A01-015D	0.7705	0.0708	0.0100	236	0.9998	11.89	0.5646	–	0.0038
A01-016D	0.8132	0.0642	0.0110	254	1.0214	12.10	0.5420	0.0035	0.0054
A01-O17L	1.3492	0.1065	0.0355	491	1.7009	9.04	0.4307	–	0.0531
A01-018D	0.7671	0.0370	0.0078	208	0.8867	12.57	0.4499	–	0.0000
A01-019D	0.7607	0.0478	0.0163	418	0.9177	12.53	0.4223	–	–
A01-020L	1.3281	0.0593	0.0586	892	1.5305	8.77	0.5124	0.0069	0.0222
A01-021D	0.9407	0.0704	0.0171	345	1.1706	10.71	0.5588	0.0023	0.0139
A01-022D	0.8523	0.0699	0.0107	234	1.0787	11.99	0.5614	–	–
A01-023D	0.8403	0.0781	0.0133	287	1.0942	11.96	0.6159	–	–
A01-024D	0.7716	0.0668	0.0120	287	0.9888	12.06	0.5920	–	–
A01-025D	0.8285	0.0624	0.0099	227	1.0305	11.72	0.5713	–	0.0154
A01-026D	0.8351	0.0596	0.0185	423	1.0309	11.76	0.5061	0.0029	0.0029
A01-027D	0.8408	0.0814	0.0144	307	1.1059	12.00	0.5995	–	–
A01-028D	0.8106	0.0884	0.0123	265	1.0975	11.99	0.5740	–	–
A01-029D	0.8003	0.0772	0.0172	385	1.0532	12.02	0.6401	–	0.0032
A01-030D	0.8600	0.0834	0.0070	147	1.1284	12.01	0.6222	0.0039	–
A01-031D	0.8165	0.1039	0.0114	234	1.1530	12.02	0.5187	0.0036	0.0236
A01-032D	0.7693	0.2430	0.0162	246	1.5569	12.40	0.5721	–	0.0090
A01-033D	0.7337	0.0643	0.0135	337	0.9435	12.06	0.3683	–	0.0110
A01-034D	0.9365	0.0957	0.0133	252	1.2468	11.29	0.6149	–	0.0026
A01-035D	0.8007	0.0738	0.0100	227	1.0396	12.47	0.4944	–	–
A01-036D	0.7826	0.0657	0.0112	266	0.9959	12.47	0.4613	–	0.0039

Table 3. Electron microprobe analyses (wt.%) of zircon and allanite in granitic gneiss. Age: apparent age in Ma, UO_2*: measured UO_2 plus UO_2 equivalent of the measured ThO_2, ThO_2*: measured ThO_2 plus ThO_2 equivalent of the measured UO_2, L and D: lighter and darker domains on BSE images of A01 allanite grain.

	ThO_2	UO_2	PbO	Age	UO_2*	CaO	Y_2O_3	S	K_2O
Z01-01	0.0076	0.0120	–	0	0.0000	0.0066	0.1088	–	–
Z01-02	0.0089	0.0293	–	0	0.0000	0.0037	0.1357	–	–
Z01-03	0.0087	0.0433	0.0056	845	0.0459	0.0093	0.1352	–	–
Z01-04	0.0195	0.0702	0.0110	988	0.0759	0.0000	0.1786	0.0079	0.0036
Z01-05	0.0262	0.2017	0.0253	837	0.2094	0.0092	0.1243	–	0.0084
Z01-06	0.0052	0.2026	0.0280	940	0.2041	0.0048	0.0462	–	0.0052
Z01-07	0.0255	0.1386	0.0175	830	0.1461	0.0053	0.2435	0.0051	–
Z01-08	0.0872	0.3356	0.0281	554	0.3619	0.0251	0.3214	0.0045	0.0136
Z01-09	0.0446	0.2256	0.0285	828	0.2387	0.0127	0.2982	0.0080	0.0089
Z01-10	0.0082	0.2977	0.0390	895	0.3001	0.0093	0.0804	0.0044	0.0032
Z01-11	0.0468	0.1061	0.0068	409	0.1204	0.0049	0.2361	–	–
Z01-12	0.0592	0.1658	0.0229	863	0.1832	0.0080	0.2816	0.0041	–
Z01-13	0.0177	0.0619	0.0098	995	0.0670	0.0073	0.1650	0.0046	0.0036
Z01-14	0.0190	0.0737	0.0092	806	0.0793	0.0122	0.2145	–	–
Z01-15	0.0149	0.0448	0.0066	921	0.0492	0.0000	0.1807	–	0.0065
Z01-16	0.0514	0.1253	0.0159	788	0.1405	0.0028	0.2731	–	0.0046
Z01-17	0.0512	0.1595	0.0208	826	0.1746	0.0116	0.3713	–	–
Z01-18	0.0089	0.1036	0.0133	865	0.1062	0.0032	0.1093	–	–
Z01-19	0.0029	0.0398	–	0	0.0000	0.0151	0.0000	–	0.0054
Z01-20	0.0059	0.1789	0.0123	489	0.1807	0.0075	0.0168	–	–
Z01-21	0.0276	0.1091	0.0148	871	0.1172	0.0074	0.1168	–	–
Z01-22	0.0062	0.2837	0.0144	367	0.2856	0.0336	0.1257	–	–
Z01-23	0.0000	0.0246	–	0	0.0000	0.0043	0.5958	0.0081	0.0208
Z01-23	0.0160	0.1861	–	0	0.0000	0.1212	2.6158	–	0.0459
Z01-24	0.1534	0.6645	0.0228	236	0.7119	0.1954	4.4915	0.0328	0.0039
Z01-25	0.0105	0.0446	0.0063	908	0.0477	0.0099	0.0367	–	0.0038
Z02-01	0.0391	0.0815	0.0127	937	0.0929	0.0049	0.2556	–	–
Z02-02	0.0045	0.1230	0.0156	866	0.1243	0.0081	0.0234	0.0041	–
Z02-03	0.0121	0.1248	0.0185	983	0.1283	0.0099	0.0684	–	0.0052
Z02-04	0.0041	0.1160	0.0089	542	0.1172	–	0.0237	–	–
Z02-05	0.0179	0.0475	0.0064	840	0.0528	0.0081	0.2698	–	–
Z02-06	0.0094	0.0358	–	0	0.0000	0.0044	0.1301	0.0054	0.0090
Z02-07	0.0299	0.0437	0.0073	953	0.0524	0.0075	0.3408	0.0069	0.0033
Z02-08	0.0075	0.0837	0.0095	771	0.0859	0.0079	0.0204	0.0052	0.0078
Z02-09	0.0165	0.1078	0.0156	948	0.1126	0.0034	0.1369	–	0.0102
Z02-10	0.0066	0.0184	0.0000	0	0.0000	0.0079	0.1811	–	0.0068
Z02-11	0.0159	0.0880	0.0063	488	0.0928	–	0.0048	–	0.0044
Z02-12	0.0072	0.0828	0.0046	393	0.0850	–	0.0091	–	0.0089
Z02-13	0.0596	0.1302	0.0150	712	0.1479	0.0042	0.1915	–	0.0056
Z03-01	0.0048	0.0137	–	0	–	0.0144	0.1273	0.0045	0.0163
Z03-02	0.0041	0.0211	–	0	–	7.9818	0.4409	–	0.0027
Z03-03	0.0080	0.0065	–	0	–	0.0111	0.3024	–	0.0106
Z03-04	0.0050	0.0088	–	0	–	0.0089	0.1285	–	0.0058
Z03-05	0.0065	0.0036	–	0	–	0.0040	0.1047	–	–
Z03-06	0.0086	0.0731	0.0105	950	0.0756	–	0.2046	–	0.0030
Z04-01	0.0135	0.0263	–	0	0.0000	0.0077	0.3952	–	0.0089
Z04-02	0.0028	0.0132	0.0000	0	0.0000	0.0086	0.1160	–	–
Z04-03	0.0297	0.0540	0.0053	598	0.0629	0.0362	0.2049	–	0.0044
Z04-04	0.0051	0.0127	–	0	0.0000	0.0047	0.2130	–	0.0074
Z04-05	0.0098	0.0374	0.0056	952	0.0403	0.0078	0.3104	–	0.0271
Z04-06	0.0030	0.0174	–	0	0.0000	0.0029	0.0000	0.0062	0.0125
Z04-07	0.0030	0.0289	–	0	0.0000	–	0.0000	0.0053	0.0055
Z04-08	0.0041	0.0844	0.0106	856	0.0856	–	0.0119	–	–

Table 3. (continued)

	ThO_2	UO_2	PbO	Age	ThO_2*	CaO	Y_2O_3	S	K_2O
A01-037L	1.4452	0.0939	0.0598	792	1.7629	8.90	0.5524	–	0.0331
A01-038D	1.2291	0.1148	0.0155	229	1.6007	9.34	0.6406	0.0029	0.0062
A01-039D	1.1016	0.0984	0.0246	407	1.4245	10.20	0.5523	0.0040	–
A01-040L	1.8496	0.0904	0.0829	894	2.1581	8.59	0.5577	0.0076	0.0230
A01-041L	1.3939	0.0693	0.0633	904	1.6306	10.06	0.5507	0.0108	0.0224
A01-042L	1.4726	0.0658	0.0626	860	1.6965	9.67	0.5581	0.0062	0.0142
A01-043L	1.4145	0.0760	0.0578	807	1.6720	9.40	0.5801	0.0045	0.0128
A01-044D	0.6936	0.0622	0.0162	425	0.8980	12.17	0.4140	0.0024	0.0274
A01-045D	0.6701	0.0699	0.0185	483	0.9008	13.82	0.4875	–	0.0598
A01-046D	0.8799	0.0866	0.0135	275	1.1612	11.59	0.6612	0.0038	0.0110
A01-047L	1.1931	0.0721	0.0553	895	1.4392	10.26	0.5264	0.0063	0.0347
A01-048D	0.0030	0.0699	0.0061	613	0.2361	3.04	0.0000	–	0.0800
A01-049D	0.0513	0.0838	–	–	0.0000	2.88	0.0000	–	0.1225
A01-050L	1.4850	0.0892	0.0661	861	1.7886	8.78	0.5388	0.0054	0.0119
A01-051L	1.5966	0.1021	0.0697	836	1.9434	8.02	0.5159	0.0039	0.0076
A01-052D	1.1898	0.0843	0.0156	252	1.4632	9.36	0.5179	0.0078	0.0086
A01-053D	0.5802	0.1970	0.0116	225	1.2177	8.83	0.5262	0.0030	0.1656
A01-054L	1.0918	0.0921	0.0319	536	1.3970	9.88	0.5050	–	0.0088
A01-055D	0.7297	0.0896	0.0158	364	1.0227	12.52	0.5865	–	0.0034
A01-056L	1.2138	0.0986	0.0378	575	1.5416	9.24	0.5210	0.0026	0.0088
A01-057L	1.3902	0.1125	0.0650	855	1.7729	8.77	0.5929	0.0029	0.0121
A01-058L	1.1005	0.1071	0.0465	744	1.4615	9.27	0.5501	0.0048	0.0126
A01-059L	0.9609	0.0929	0.0320	591	1.2701	10.43	0.5200	0.0046	0.0087
A01-060L	1.4965	0.1179	0.0707	868	1.8980	8.74	0.5604	–	0.0079
A01-061L	1.5507	0.1382	0.0731	844	2.0204	8.28	0.5500	0.0055	0.0073
A01-062L	1.2252	0.0814	0.0499	777	1.5003	9.74	0.2735	–	0.0077
A01-063D	0.8920	0.1045	0.0064	123	1.2277	11.12	0.5678	–	0.0100
A01-064D	0.8435	0.0990	0.0087	177	1.1628	11.86	0.5790	–	0.0042
A01-065D	0.7083	0.0651	0.0092	237	0.9192	11.90	0.4990	–	0.0065
A01-066D	0.7538	0.1021	0.0193	417	1.0890	12.74	0.4054	–	0.0018
A01-067D	0.6700	0.0770	0.0057	147	0.9178	12.20	0.4385	–	0.0000
A01-068D	0.7657	0.0979	0.0075	164	1.0811	11.82	0.5279	–	0.0045
A01-069D	0.5678	0.0409	0.0160	534	0.7033	4.94	0.3591	0.0042	0.0092
A01-070D	1.0192	0.0895	0.0237	425	1.3133	9.95	0.4385	0.0085	0.0054
A01-071D	1.1532	0.0826	0.0276	456	1.4252	9.33	0.4621	0.0079	0.0121
A01-072D	0.6117	0.0543	0.0059	177	0.7868	14.08	0.4455	0.0000	0.0063
A01-073D	1.1259	0.0866	0.0204	342	1.4086	9.39	0.5021	0.0078	0.0000
A01-074D	1.1717	0.0723	0.0169	284	1.4067	9.43	0.4807	0.0062	0.0056
A01-075D	1.1607	0.0799	0.0157	261	1.4200	9.20	0.4920	0.0061	0.0076
A01-076D	1.0640	0.0788	0.0138	247	1.3194	9.56	0.5221	0.0052	0.0063
A01-077D	1.1514	0.0773	0.0164	276	1.4025	9.23	0.4820	0.0053	0.0081
A01-078L	1.3767	0.1523	0.0684	842	1.8942	9.57	0.4959	0.0032	0.0122
A01-079L	0.9522	0.0509	0.0426	881	1.1257	10.76	0.4302	0.0095	0.0027
A01-080L	1.0991	0.0719	0.0503	872	1.3440	10.13	0.5520	0.0138	0.0221
A01-081D	1.2357	0.1504	0.0158	217	1.7222	9.62	0.6111	0.0039	0.0200
A01-082D	1.0064	0.1141	0.0140	240	1.3761	9.19	0.5355	0.0052	0.0159
A01-083L	1.1940	0.0989	0.0361	557	1.5223	9.96	0.5972	0.0059	0.0078
A01-084D	1.1856	0.0831	0.0144	234	1.4547	10.15	0.5930	0.0000	0.0087
A01-085D	1.4417	0.1031	0.0186	247	1.7759	9.33	0.5314	0.0083	0.0081
A01-086D	0.9026	0.0706	0.0217	450	1.1350	9.29	0.4852	0.0048	0.0101
A01-087D	0.7385	0.0634	0.0092	230	0.9438	11.38	0.5812	0.0057	0.0067
A01-088D	0.8010	0.0873	0.0170	369	1.0866	10.67	0.4141	0.0025	0.0163
A01-089D	1.0885	0.0799	0.0247	430	1.3511	8.74	0.4953	0.0051	0.0075
A01-090D	1.0653	0.0818	0.0161	286	1.3312	8.85	0.5249	0.0045	0.0000
A01-091D	0.8888	0.0717	0.0087	184	1.1201	8.34	0.5251	0.0026	0.0245
A01-092D	1.0631	0.0747	0.0137	248	1.3053	9.23	0.5016	0.0098	0.0045

Table 3. (continued)

	ThO_2	UO_2	PbO	Age	ThO_2*	CaO	Y_2O_3	S	K_2O
A01-093L	0.9603	0.0955	0.0287	528	1.2766	9.33	0.5094	0.0000	0.0276
A01-094D	1.0572	0.0755	0.0143	259	1.3022	9.20	0.5218	0.0051	0.0212
A01-095D	1.0530	0.0860	0.0240	423	1.3355	9.05	0.5591	–	0.0089
A01-096L	1.3076	0.1054	0.0607	849	1.6660	8.51	0.5586	0.0089	0.0204
A01-097L	1.3128	0.0974	0.0617	874	1.6447	8.33	0.5319	0.0028	0.0258
A01-098L	1.2595	0.0750	0.0547	842	1.5143	8.26	0.5066	0.0076	0.0196
A01-099L	1.3080	0.0835	0.0579	848	1.5919	8.40	0.5214	0.0097	0.0149
A01-100L	1.2209	0.0645	0.0523	847	1.4402	8.66	0.5246	0.0071	0.0050
A01-101L	0.9190	0.0663	0.0345	707	1.1418	9.75	0.4355	0.0027	0.0120
A01-102L	1.1985	0.0830	0.0536	844	1.4806	8.83	0.4755	0.0066	0.0092
A01-103L	1.1033	0.0784	0.0422	722	1.3670	8.77	0.4985	0.0087	0.0118
A01-104L	1.0359	0.0844	0.0350	623	1.3176	8.89	0.5379	0.0042	0.0102
A01-105L	1.1235	0.0894	0.0541	882	1.4283	8.55	0.5195	0.0040	0.0071
A01-106L	1.3199	0.0897	0.0600	860	1.6252	8.06	0.5211	0.0076	0.0226
A01-107L	1.1317	0.0899	0.0601	970	1.4406	8.60	0.5483	–	0.0283
A01-108L	1.0578	0.0786	0.0412	728	1.3224	8.46	0.5655	–	0.0118
A01-109L	1.2000	0.0781	0.0503	802	1.4645	8.59	0.5251	–	0.0100
A01-110D	1.1748	0.0810	0.0263	430	1.4410	8.61	0.5111	0.0035	0.0118
A01-111D	1.1468	0.0810	0.0266	443	1.4133	8.43	0.5050	0.0044	0.0119
A01-112L	1.2400	0.0762	0.0429	672	1.4953	8.84	0.5461	0.0051	0.0076
A01-113D	1.1938	0.0874	0.0300	476	1.4821	8.13	0.4381	0.0110	0.0269
A01-114L	1.1504	0.0999	0.0348	551	1.4819	8.38	0.4829	0.0077	0.0310
A01-115D	1.2072	0.0876	0.0308	484	1.4963	8.51	0.4914	0.0074	0.0256
A01-116L	1.2354	0.0869	0.0406	624	1.5254	8.58	0.4927	0.0091	0.0280
A01-117L	1.2147	0.0582	0.0413	686	1.4099	8.47	0.5030	0.0106	0.0275
A01-118L	1.3489	0.0897	0.0590	832	1.6534	7.83	0.5890	0.0083	0.0508
A01-119L	1.3854	0.0987	0.0695	938	1.7235	8.58	0.5156	0.0092	0.0480
A01-120L	1.3153	0.0852	0.0601	872	1.6055	8.83	0.5326	0.0023	0.0140
A01-121L	1.2715	0.0735	0.0625	954	1.5237	8.45	0.5312	0.0024	0.0236
A01-122L	1.2429	0.1671	0.0514	668	1.8026	7.32	0.3882	0.0068	0.0985
A01-123L	1.4320	0.1032	0.0549	722	1.7792	8.27	0.4501	0.0048	0.0219
A01-124D	0.8281	0.0899	0.0089	188	1.1183	10.78	0.6064	–	0.0125
A01-125D	0.8281	0.0899	0.0121	255	1.1197	10.78	0.6064	–	0.0125
A01-126D	0.6394	0.0574	0.0093	266	0.8257	11.87	0.4751	–	0.0055
A01-127L	0.9754	0.0490	0.0440	897	1.1427	9.84	0.5958	0.0081	0.0208
A01-128D	1.2173	0.0947	0.0168	260	1.5246	8.70	0.5674	0.0083	0.0127
A01-129D	0.6783	0.0812	0.0100	251	0.9416	11.56	0.6038	0.0024	–
A01-130D	0.6963	0.0828	0.0108	264	0.9650	11.46	0.6023	–	0.0022
A01-131D	0.9537	0.0785	0.0242	469	1.2125	9.60	0.5223	0.0050	0.0213
A01-132D	0.7026	0.0609	0.0085	223	0.8997	11.65	0.6457	–	0.0051
A02-001core	0.6250	0.0521	0.0162	478	0.7969	13.77	0.5578	–	0.0036
A02-002core	0.5792	0.0864	0.0157	428	0.8631	14.14	0.5157	–	0.0026
A02-003core	0.5765	0.1737	0.0243	497	1.1504	12.40	0.5298	0.0117	0.0473
A02-004core	0.5165	0.0657	0.0110	355	0.7312	14.40	0.4196	–	0.0050
A02-005rim	0.5336	0.0780	0.0081	243	0.7864	14.38	0.6733	–	0.0040
A02-006rim	0.5944	0.0871	0.0084	227	0.8763	13.74	0.5218	–	0.0076
A02-007rim	0.5739	0.0887	0.0085	233	0.8611	14.11	0.5598	–	0.0083
A02-008rim	0.5456	0.0795	0.0069	203	0.8025	14.16	0.5130	–	–
A02-009rim	0.5238	0.0934	0.0099	283	0.8274	14.25	0.6482	–	–
A03-001core	0.6280	0.0321	0.0142	455	0.7337	12.95	0.3300	–	–
A03-002core	0.4908	0.0833	0.0138	425	0.7645	14.46	0.3469	–	0.0081
A03-003rim	0.8242	0.1044	0.2643	4059	–	11.64	0.5957	0.0650	0.0122
A03-004rim	0.8264	0.0384	0.2778	5157	–	11.27	0.5993	–	0.0510
A03-005rim	0.9488	0.1017	0.2605	3817	–	9.00	1.3475	0.0359	0.0158

However, the correlation between the ThO_2* and PbO (Fig. 8, right) suggests a relatively insignificant amount of initial Pb in porphyroblast A01, from which most analyses were obtained. As for zircon, analyses on allanite grain cores are arbitrarily separated with a threshold of 750 Ma. The data points with older apparent ages (open squares) tend to be more Th rich, and yield a poorly defined isochron of 825±110 Ma. Allanite rims give variable apparent ages, with younger spots tend to contain high Y_2O_3 than older spots. Analyses for the rims are arbitrarily separated with thresholds of 400, 300 and 200 Ma. Data points with apparent ages older than 400 Ma (open circles) give an isochron age of 438±99 Ma. A total of 44 data points with 200–300 Ma apparent ages (solid circles) define an isochron of 254±30 Ma. Data points with apparent ages younger than 200 Ma give a poorly defined isochron of 166 Ma.

DISDCUSSION

Chronology of the Deokjeongri Granitic Gneiss

The CHIME age for concentrically-zoned and patchy zircon is 824±29 Ma. Allanite cores give an identical age of 825±110 Ma. As mentioned earlier, zircon grains from samples of the Deokjeongri Granitic Gneiss have been dated previously by SHRIMP dating and yielded consistent ages for zircon cores, ca. 815 Ma (Cho, 2001), 940–395 Ma age (mean age of 817±22 Ma, Kim *et al.*, 2006) and 839±10 Ma (Kim *et al.*, 2008). Numerous studies have shown that Th-U-Pb measurements on zircon can provide reliable ages of crystallization for protoliths of high-T gneisses, due to the high closure temperatures for Pb diffusion (*e.g.* 1000°C: Lee *et al.*, 1997; Cherniak and Watson, 2000). The 824±29 Ma CHIME age of the zircon cores is consistent with SHRIMP results, and the concentric, faceting growth zoning is typical of formation in magma. These ages are therefore interpreted as the time of emplacement for the granitic protolith.

Compositionally uniform domains with low Y_2O_3 contents discordantly overgrow concentrically-zoned cores in zircon grains Z01 and Z02 (Figs. 5 and 6). Most spots in the uniform domains contain little PbO, but several spots contain measurable PbO. Screened analyses with low CaO and K_2O contents give a poorly defined 505±125 Ma isochron. We propose that the 505±125 Ma zircon age is comparable with the 438±99 Ma allanite age within the limit of analytical uncertainty and that the absence of clearly delineated Paleozoic domains modifying Neoproterozoic zircon resulted from sluggish growth or recrystallization during a mid-grade thermal event. In contrast, allanite is more prone to modification, and in the same sample records a 438±99 Ma stage of regrowth and recrystallization that developed sizable Th-poor rims around 825±110 Ma Th-rich cores. The Paleozoic CHIME age from allanite matches ca. 420 Ma SHRIMP ages for zircon overgrowths reported by Kim *et al.* (2006) and 335–473 Ma SHRIMP ages for some zircon cores (Cho, 2001). A third, younger allanite CHIME age of 254±30 Ma is comparable with the 229 Ma age for spot 11 of zircon grain Z05, and also corresponds to multiple published SHRIMP ages (223–235 Ma, Cho, 2001; 229±10 Ma, Kim *et al.*, 2008) for zircon rims, as well as a 241.5±5.2 Ma K-Ar biotite age (Kim *et al.*, 2006). The new zircon and allanite dating confirms that the Deokjeongri Granitic Gneiss underwent both Silurian (438±99 Ma) and Permo-Triassic (254±30 Ma) thermal events after the formation of the granitic protolith at 824±29 Ma.

Relationship between the Deokjeongri Granitic Gneiss and garnet amphibolite

The granitic gneiss contains a serpentinite lens that in turn contains an amphibolite boudin, elongated in the same direction as the host gneiss (Oh *et al.*, 2004). Oh *et al.* (2004) and Kim *et al.* (2006) recognized three stages of metamorphism within the garnet amphibolite: first, an eclogite stage characterized by omphacitic pyroxene + garnet (M1); second, a granulite-facies stage characterized by augite + garnet (M2); and third, an amphibolite-facies stage characterized by amphibole + plagioclase with retrograde modification of garnet (M3). Oh *et al.* (2004) reported Sm-Nd garnet-whole rock ages of 297.9±5.7, 276.8±8.7 and 268.0±3.3 Ma from such rocks. Kim *et al.* (2006) assigned their 231 Ma SHRIMP age on zircon overgrowths to the M1 stage, and constrained the upper limit of the M3 stage by 218.5±4.8 and 207.6±4.5 Ma K-Ar biotite ages.

In our sample, allanite rims have variable Y concentrations. Spots with 200–300 Ma apparent ages tend to be richer in Y_2O_3 than those with older apparent ages. Relationships between Y contents of co-existing metamorphic minerals can provide important constraints on timing of mineral growth (*e.g.* Pyle *et al.*, 2001). Elemental mapping of a garnet grain shows an outward decrease in YLα from 75–55 cps to 35–45 cps within the low Mn core (FIg. 4). This suggests that Y in garnet was not buffered by an Y-saturated mineral such as xenotime during growth. Due to the compatibility of Y in garnet by $Y^{3+}Al^{3+} \rightleftarrows Mn^{2+}Si^{4+}$ (Jaffe, 1951) and $Y^{3+} \rightleftarrows Al^{3+}$ (Wang *et al.*, 2003) substitutions, garnet growth decreases the availability of Y within the effective bulk. Additionally, retrograde plagioclase and biotite formation at the expense of garnet occurs on the garnet margin. As plagioclase and biotite contain negligible Y (*e.g.* Pyle *et al.*, 2001), the replacement of garnet by plagioclase and biotite likely enriches Y at the garnet margin, as well as Mn, and allows the growth of tiny xenotime grains with plagioclase and biotite in the matrix.

The variation in the Y content within allanite can be attributed to the growth and breakdown of garnet. The development of ca. 250 Ma Y-rich domains in the rims of porphyroblast A01 was likely synchronous with the breakdown of garnet that originally formed in equilibrium with Y-poor older domains in allanite rims. Elongated allanite grains, as exemplified by matrix grain A02, also consist of Y-poor ca. 400 Ma and Y-rich ca. 250 Ma domains, or of Y-rich ca. 250 Ma domains alone. These occur in textural equilibrium with main constituent minerals whose alignment is consistent with that of M3 hornblende in amphibolite. This texture suggests that ca. 250 Ma domains in the rim of porphyroblastic allanite and retrograde garnet margins were formed during M3. The garnet cores likely formed at ca. 440 Ma in the granitic gneiss, whereas in the amphibolite (retrogressed eclogite) garnet cores grew during Permo-Triassic metamorphism (Oh *et al.*, 2004, 2005; Kim *et al.*, 2006, 2008). The Deokjeongri Granitic Gneiss and the garnet amphibolite (retrogressed eclogite) thus could be of differing origin, and were juxtaposed just after the M2 stage as suggested by Kim *et al.* (2006).

Geochemistry of the Deokjeongri granitic gneiss

The bulk-rock $Al_2O_3/(CaO+Na_2O+K_2O)$ value of our sample falls within the compositional range for I-type granites (Chappell and White, 1974), but the high K_2O/Na_2O

(wt%) value of 2.09 does not, being more typical of the high-K calc-alkaline series or shoshonite series (Peccerillo and Taylor, 1976). The sample falls in the within-plate granitoid field on the Rb *vs* Y + Nb tectonic discrimination diagrams of Pearce *et al.* (1984) and Pearce (1996). The granitic gneiss at Baekdong bears other characteristics of A-type granite, including a high concentration of Zr along with a low concentration of V. In contrast, tonalitic gneiss from the west of Yedang Reservior (site 2), also mapped as part of the Deokjeongri Granitic Gneiss, is typical of volcanic arc granitoids, having low concentrations of Y, Nb and Rb. The chemistry resembles closely that of the Neoproterozoic granitic gneisses described by Kim *et al.* (2008). The Neoproterozoic (841±10 and 235±13 Ma) leucogranite from the Wolhyeonri Formation also gives chemistry typical of volcanic arc granitoids (Kim *et al.*, 2008). Further, the within-plate tectonic setting of the present granitic gneiss contrasts to the island arc tectonic setting of the garnet amphibolites at Baekdong (Oh *et al.*, 2004) and sites 1, 3 and 4 (Table 2), which are plotted in the field of island arc tholeiite on the Ti/100-Zr-Y×3 diagram of Peace and Cann (1973) along with low Y (<24 ppm), Zr (<48 ppm) and TiO_2 (typically <1 wt.%) concentrations.

Neoproterozoic granitoids and their metamorphic derivatives are not typical of the Paleoproterozoic gneisses of the Gyeonggi Massif. Kim *et al.* (2008) suggested a correlation of granitic gneiss in the Hongseong area with the Taohong and Xiqiu Tonalite-Granodiorite Bodies that occur in the southwestern part of the Yangtze Craton, which have an amphibole-rich calc-alkaline affinity and formed in an active continental margin at 913±15 Ma and 905±14 Ma, respectively (Ye *et al.*, 2007). The granitic gneiss described in this paper, however, does not match either geochemically or chronologically with the Taohong and Xiqiu tonalite-granodiorite bodies. Within the vicinity of the Gyeonggi massif, only the orthogneiss host of the Yangkou ultra-high pressure complex in the Sulu Collisional Belt has an A-type affinity (Katsube *et al.*, 2009). This orthogneiss has yielded zircon core and rim ages of 801±45 Ma and 235±16 Ma, respectively (Hirajima, unpublished data, reported in Hirajima and Nakamura, 2003) and of 714±110 Ma and 226±63 Ma, respectively (Katsube *et al.*, 2009). An association of these granitoids with those at Baekdong is possible; however, the former lack evidence for the ca. 430 Ma tectonometamorphic event recorded in the latter.

The ages from the Deokjeongri Granitic Gneiss are diverse, even within single samples; ca. 815 Ma, 335–473 Ma and 223–235 Ma (Cho, 2001), 940–395 Ma and ca. 420 Ma (Kim *et al.*, 2006), 839±10 Ma and 229±10 Ma (Kim *et al.*, 2008) and 824±29 Ma, 438±99 Ma and 254±30 Ma (this study). This, and the geochemical diversity of different parts of the gneiss, is consistent with the Deokjeongri Granitic Gneiss representing a metamorphic complex formed by amalgamation of orthogneisses whose protoliths were formed in different tectonic settings during the Neoproterozoic. Further chronological and petrological characterization of the Deokjeongri Granitic Gneiss is needed to correlate the metamorphic rocks in the Hongseong area with those in the Sulu Collisional Belt in China.

Geometry of the Deokjeongri Granitic Gneiss and the Wolhyeonri Formation

The Deokjeongri Granitic Gneiss and the Wolhyeonri Formation have steeply NE or SW plunging mineral lineations with a consistent top-to-the-SW sense of shear (Fig.

2). This suggests that the Deokjeongri Granitic Gneiss and the Wolhyeonri Formation were subjected a common tectonic regime. The S-shape distribution of the Wolhyeonri Formation coupled with the lineation and shear sense leads us to a conclusion that the granitic gneiss was subjected to a compressional regime that resulted in tight large-scale folding, as illustrated in the block diagram in Fig. 9. The lineation in amphibolite (retrogressed eclogite) is defined by the alignment of amphibole, and therefore postdates the transformation of eclogite into amphibolite. Evidently, the Deokjeongri Granitic Gneiss and the Wolhyeonri Formation behaved as a coherent unit during exhumation.

SHRIMP dating of zircon rims by Kim *et al.* (2008) revealed that the adjacent Paleoproterozoic Yugu Granitic Gneiss (1.88–1.86 Ga) was regionally metamorphosed during the Triassic, at ca. 235 Ma. This age is indistinguishable from the 229±10 Ma rim age of zircon in the amphibole-bearing orthogneiss from Baekdong (Kim *et al.*, 2008) and the 231±3.3 Ma rim age of zircon in the retrogressed eclogite (Kim *et al.*, 2006). Kim *et al.* (2008), therefore, correlated ca. 235 Ma metamorphism of the Yugu Granitic Gneiss and the Deokjeongri Granitic Gneiss with the Triassic collisional event marked by the retrogression of eclogite in the Hongseong area (Oh *et al.*, 2002, 2005; Guo *et al.*, 2004). However, an earlier Silurian metamorphic event can now be identified in the Deokjeongri Granitic Gneiss (438±99 Ma), associated with the growth of Ca-rich garnet.

The Yugu Granitic Gneiss and the banded gneiss show a consistent top-to-the-NE shear sense with gently inclined NE-SW mineral alignments (Fig. 2). This is different from the sense of mineral lineation in the Deokjeongri Granitic Gneiss and the Wolhyeonri Formation. Furthermore, the Yugu Granitic Gneiss does not show any evidence of high-pressure metamorphism. To explain the contrasting shear sense and tectonic history, we adopt an allochthon model that the high-pressure Wolhyeonri Formation and the Deokjeongri Granitic Gneiss became a coherent block by amalgamation and were juxtaposed with the Yugu Granitic Gneiss by NE-ward thrusting (Fig. 9a). The NE-SW lineation with top-to-the-NE shear sense in the Yugu Granitic Gneiss is ascribable to

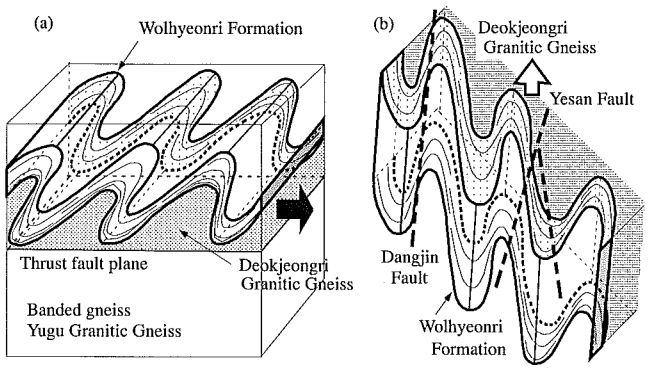

Fig. 9 (a) Over-thrusting model for the juxtaposition of the Deokjeongri Granitic Gneiss and Wolhyeonri Formation with the Yugu Granitic Gneiss. (b) Formation of the SW-ward shear by tilting and differential exhumation.

this thrust, as is the sinistral rotation of the hornblende-rich block (Fig. 3a) in the metasediment lens at sampling site 5. Suzuki (2009) proposed contact metamorphism by a hot allochthon as the cause of a Permo-Triassic low-pressure thermal overprint on the Paleoproterozoic (1.86 Ga) granitic granulite in the Hwacheon area. Subsequent gravitational relaxation resulted in a significant tilting of piled-up crust between the Dangjin and Yesan Faults, reorienting macrofolds and stretching lineations. The SW shear sense is thus due to the differential exhumation of the Deokjeongri Granitic Gneiss relative to the Wolhyeonri Formation (Fig. 9b).

CONCLUSION

(1) The sample of the Deokjeongri Granitic Gneiss exposed at Baekdong (36°33.521'N, 126°44.131'E) gives consistent zircon and allanite core ages of 824±29 Ma and 825±110 Ma, respectively. This age is interpreted as the time of formation of a magmatic protolith. Allanite rims ages of 438±99 Ma for Y-poor spots and 254±30 Ma for Y-rich spots likely date two tectonothermal events, with the formation of Ca-rich garnet in the former and Mn-rich garnet rims in the latter.

(2) The age spectrum within the sample is inconsistent with the age spectra reported by Cho (2001), Kim *et al.* (2006) and Kim *et al.* (2008). Further, the within-plate affinity of the present sample is contrary to the volcanic arc affinity of samples described by Kim *et al.* (2008). The diversity in age spectra and tectonic setting of protolith formation provide evidence for the formation of the Deokjeongri Granitic Gneiss from differing orthogneisses with different tectonothermal histories. The absence of Permo-Triassic ultra-high pressure metamorphism in the present granitic gneiss suggests a post-eclogite stage amalgamation of the Deokjeongri Granitic Gneiss and the Wolhyeonri Formation.

(3) The Deokjeongri Granitic Gneiss and the Wolhyeonri Formation together underwent large scale folding. The compressional regime is attributable to the juxtaposition of these lithologies against the Paleoproterozoic Yugu Granitic Gneiss by NE-ward thrusting.

ACKNOWLEDGMENTS

We would like to thank Dr. M. Takeuchi and Dr. T. Imayama for their constructive reviewing of the manuscript and Professor M. Enami, Dr. S. Wallis and Dr. T. Kato for their comments on the first draft. This work was supported by Grant-in-Aid for Scientific Research (C) (No. 21540471) from Japan Society for the Promotion of Science.

REFERENCES

Adachi, K., Suzuki, K. and Nagasawa, K. (1998): Vermiculitization process of biotite from the Shinshiro tonalite in the eastern part of Aichi Prefecture, central Japan. *Nendo Kagaku (Journal of the Clay Science Society of Japan)*, **38**, 103–112.

Chappell, B.W. and White, A.J.R. (1974): Two contrasting granite types. *Pacific Geology.* **8**, 173–174.

Cherniak, D.J. and Watson E.B. (2000): Pb diffusion in zircon. *Chemical Geology*, **172**, 5–24.

Cho, M. (2001): A continuation of Chinese ultrahigh-pressure belt in Korea: evidence from ion microprobe U-Pb zircon ages. *Gondwana Research*, **4**, 748.

Dunn, P.J. (1985): The lead silicates from Franklin, New Jersey: occurrence and composition. *Mineralogical Magazine*, **49**, 721–727.

Geisler, T. and Schleicher, H. (2000): Improved U-Th-total Pb dating of zircons by electron microprobe using a simple new background modelling procedure and Ca as a chemical criterion of fluid-induced U-Th-Pb discordance in zircon. *Chemical Geology*, **163**, 269–285.

Guo, J.H., Zhai, M., Oh, C.W. and Kim. S.W. (2004): 230 Ma eclogite from Bibong, Hongseoung area, Gyeonggi Massif, South Korea: HP metamorphism, zircon SHRIMP U-Pb ages, and tectonic implication. *Abstract volume of International association for Gondwana Research, South Korea Chapter, Miscellaneous Pbl.* pp.11–12, 2 December 2004, Chonju.

Hirajima, T. and Makamura, D. (2003): The Dabie Shan-Sulu orogen. *In (Carswell, D.A. amd Compagnoni, R. ed) Ultra-high pressure metamorphism, EMU note in mineralogy*, Chapter 5, 105–144, CD-Rom 5th EMU School of Mineralogy Budapest, Hungary (July 21–25, 2003) .

Jaffe, H.W. (1951): The role of yttrium and other minor elements in the garnet group. *American Mineralogist*, **36**, 133–155.

Katsube, A., Hayasaka, Y., Santosh, M. Li, S. and Terada, K. (2009): SHRIMP zircon U-Pb ages of eclogite and orthogneiss from Sulu ultrahigh-pressure zone in Yangkou area, eastern China, *Gondwana Research*, **15**, 168–177.

Kato, T., Enami, A. and Zhai, M. (1997): Ultrahigh-pressure marble and eclogite in the Su-Lu ultrahigh-pressure terrane, eastern China. *J. Metamorphic. Geol.* **15**, pp. 169–182

Kim S.W., Oh, C.W., Williams, I.S., Rubatto, D., Ryu, I.C., Tajesh, V.J., Kim, C.B. Guo, J. and Zhai, M. (2006): Phanerozoic high-pressure eclogite and intermediate-pressure granulite faces metamorphism in the Gyeonggi Massif, South Korea: Implications for the eastward extension of the Dabie-Sulu continental collision zone. *Lithos*, **92**, 357–377.

Kim S.W., Williams, I.S., Kwon, S. and Oh, C.W. (2008): SHRIMP zircon geochronology, and geochemical characteristicx of metamorphic rocks from the south-western Gyeonggi Block, Korea: Implications for Paleoproterozoic to Mesozoic tectonic links between the Korean Peninsula and eastern Chine. *Precambrian Research*, **162**, 475–497.

Leake, B.E., Woolley, A.R., Arps, C.E.S., Birch, W.D., Bilbert, M.C., Grice, J.D., Hawthome, F.C., Kato, A., Kisch, H.J., Krivovivhes, V.G., Kinthout, K., Laird, J. and Mandarino, J. (1997): Nomenclature of amphiboles. Report of the Subcommittee on Amphiboles of the International Mineralogical Association Commission on New Minerals and Mineral Nales. *Mineralogical Magazine*, **60**, 259–321.

Lee, B.J., Kim, D.H., Choi, H.I., Kee, W.S. and Park, K.H. (1996): Explanatory note of the Daejeon Sheet at 1:250,000. Korean Institute of Geology, mining and Materials, 59p.

Lee, J.K., Williams, I.S. and Ellis, D.J. (1997): Pb, U and Th diffusion in natural zircon. *Nature*, **390**, 159–162.

Oh, C.W., Choi, S.G., Zhai, M. and Guo, J. (2002): The first finding of eclogite relict in the Korean Peninsula and its tectonic modeling. Proceedings of International Symposium Celebrating 55th Anniversary of the Geological Society of Korea, P. 7.

Oh, C.W., Choi, S.G. Song, S.H. and Kim. S.W. (2004): Metamorphic evolution of the Baekdong Metabasite in the Hongseong area, South Korea and its relationship with the Sulu collision belt of China. *Gondwana Research*, **7**, 809–816.

Oh, C.W., Kim, S.W., Choi, S.G., Zhai, M., Guo, J. and Sajeev, K. (2005): First finding of eclogite facies metamorphism event in South Korea and its correlation with the Dabie-Sulu Collision Belt in China. *Journal of Geology*, **113**, 226–232.

Oh, C.W., Kim. S.W. and Williams, I. (2006): Late Pwemian HT spinel granulite in Korea and its tectonic implications for the collision between the North ans South China Blocks. *Lithos*, **92**, 557–575.

Oh, C.W., Choi, S.-G., Seo, J., Rajesh, V.J., Lee, J.H., Zhai, M. and Peng, P. (2009): Neoproterozoic tectonic evolution of the Hongseong area, southwestern Gyeonggi Massif, South Korea; implication for the tectonic evolution of Northeast Asia. *Gondwana Research*, **16**, 272–284.

Pearce, J.A. (1996): Sources and setting of granitic rocks. *Episodes*, **19**, 120–125.

Pearce, J.A. and Cann, J.R. (1973); Tectonic setting of basic volcanic rocks determined using trace element analyses. *Earth and Planetary Science letters*, **19**, 290–300.

Pearce, J.A., Harris, N.B. W. and Tindle A.G. (1984): Trace element discrimination diagrams for the tectonic interpretation of granitic rocks. *Journal of Petrology*, **25**, 956–983.

Peccerillo, A. and Taylor, S.R. (1976): Geochemistry of Eocene calc-alkaline volcanic rocks from the Kastamonu area, Northern Turkey. *Contributions to Mineralogy and Petrology*, **58**, 68–81.

Pyle, J.M., Spear, F.S., Rudnick, R.L. and McDonough, W.F. (2001): Monazite-xenotime-garnet equilibrium in metapelites and a new monazite-garnet thermometer. *Journal of Petrology*, **42**, 2083–2107.

Seo, J., Choi, S.G. and Oh, C.W. (2010): Petrology, geochemistry, and geochronology of the post-collisional Triassic mangerite and syenite in the Gwangcheon area, Hongseong Brlt, South Korea. *Gondwana Research*, **18**, 479–496.

Suzuki, K. (2009): CHIME dating and age mapping of monazite in granulites and paragneisses from the Hwacheon area, Korea: implications for correlations with Chinese cratons. *Geosciences Journal*, **13**, 275–292.

Suzuki, K. and Adachi, M. (1991): Precambrian provenance and Silurian metamorphism of the Tsubonosawa paragneiss in the South Kitakami terrane, Northeast Japan, revealed by the chemical Th-U-total Pb isochron ages of monazite, zircon and xenotime. *Geochemical Journal*, **25**, 357–376.

Suzuki, K., Adachi, M. and Tanaka, T. (1991): Middle Precambrian provenance of Jurassic sandstone in the Mino Terrane, central Japan: Th-U-total Pb evidence from an electron microprobe monazite study. *Sedimentary Geology*, **75**, 141–147.

Suzuki, K. and Kato, T. (2008): CHIME dating of monazite, xenotime, zircon and polycrase: protocol, pitfalls and chemical criterion of possibly discordant age data. *Gondwana Research*, **14**, 569–586.

Wang, R.-C., Hu, H.-A., Zhang, A.-C., Xu, S.-J. and Wang. D.-Z. (2003): Yttrium zoning in garnet from the Xihuashan granite complex and its petrological implications. *Chinese Science Bulletin*, **48**, 1611–1615.

Wang, X.M., Liou, J.G. and Mao, H.K. (1989): Coesite-bearing eclogites from the Dabie mountains in central China. *Geology* **17**, 1085–1088.

Ye, M.F., Li, X.H., Li, W.X., Liu, Y. and Li, Z.X. (2007): SHRIMP zircon U-Pb geochronogical and whole-rock geochemical evidence for an early Neoproterozoic Sibaoan magmatic arc along the southeastern margin of the Yangtze Block. *Gondwana Research*, **12**, 144–156.

Zhang, R.Y., Liou, J.G. and Cong, B. (1994): Petrogenesis of garnet-bearing ultramafic rocks and associated eclogites in the Su-Lu ultrahigh-P metamorphic terrane, eastern China. *Journal of Metamorphic Geology*, **12**, 169–186.